

Multi-Tech Sensing In-Field Demonstration on Terrestrial Optical Data Networks

Original

Multi-Tech Sensing In-Field Demonstration on Terrestrial Optical Data Networks / Virgillito, E., Notarstefano, F., Ambrosone, R., Malik, G., Straullu, S., Bratovich, R., Corsini, R., Herrero, A., Hovsepyan, M., Carpentieri, F., Donadello, S., Clivati, C., Curri, V.. - In: JOURNAL OF OPTICAL COMMUNICATIONS AND NETWORKING. - ISSN 1943-0620. - (2026), pp. 37-48. [10.1364/JOCN.590101]

Availability:

This version is available at: 11583/3010947 since: 2026-05-18T09:52:41Z

Publisher:

Optica Publishing Group

Published

DOI:10.1364/JOCN.590101


Terms of use:

This article is made available under terms and conditions as specified in the corresponding bibliographic description in the repository

Publisher copyright

(Article begins on next page)

Multi-tech sensing in-field demonstration on terrestrial optical data networks

EMANUELE VIRGILLITO,^{1,*}  FEDERICO NOTARSTEFANO,^{1,2} RENATO AMBROSONE,¹ 
GULMINA MALIK,¹  STEFANO STRAULLU,³  RUDI BRATOVICH,⁴ RAFFAELE CORSINI,⁴
ANDRÉ HERRERO,⁵ MARIANNA HOVSEPYAN,⁶ FRANCESCO CARPENTIERI,⁶
SIMONE DONADELLO,²  CECILIA CLIVATI,²  AND VITTORIO CURRI¹ 

¹Politecnico di Torino, Corso Duca degli Abruzzi, 24, Torino, Italy

²INRIM, Strada delle Cacce, 91, Torino, Italy

³LINKS Foundation, Torino, Italy

⁴SM-Optics, Cologno Monzese, Italy

⁵INGV, Roma, Italy

⁶Open Fiber, Roma, Italy

*emanuele.virgillito@polito.it

Received 5 February 2026; revised 14 April 2026; accepted 15 April 2026; published 4 June 2026

Transforming optical transport networks into a distributed sensing grid is a promising pathway to enhance infrastructure resilience and environmental awareness. To achieve widespread scalability without disrupting data traffic, operators can exploit the synergy between different sensing techniques naturally coexisting on the same infrastructure. In this paper, we present an in-field demonstration of a multi-technique sensing framework operating on live terrestrial optical networks, combining interferometric phase sensing and state of polarization (SOP) monitoring. We first propose and validate an unsupervised anomaly detection pipeline based on autoencoders, applied to a 38 km regional link connecting Ascoli Piceno and Teramo (Italy), and show some examples of detected events. This framework proves capable of automatically identifying signal anomalies across different physical observables without relying on manual labeling. Subsequently, we move to a metropolitan urban scenario in the city of Turin and assess a multi-tech sensing analysis using coherent transceivers and state-of-polarization metrics obtained from polarimeters and a cost-effective polarization beam splitter-based device. We highlight the correlation between specific sensing metrics and standard network telemetry data, such as the bit error rate (BER) and temperature, and validate the system's capability to detect mechanical perturbations originating from human activity along the cable or from controlled experiments using a robotic arm. These results confirm the feasibility of aggregating heterogeneous data sources into a unified sensing plane to enable pervasive infrastructure supervision. © 2026 Optica Publishing Group under the terms of the [Optica Open Access Publishing Agreement](#)

[Agreement](#)

<https://doi.org/10.1364/JOCN.590101>

1. INTRODUCTION

Optical fiber networks constitute the critical backbone of modern digital society, supporting global communication and data exchange. Due to the growth in bandwidth demand, these infrastructures have become pervasive, densely covering large geographical areas with thousands of kilometers of optical cables. In this context, the integrity and reliability of the physical layer are becoming a priority for operators and institutions [1]. However, the infrastructure's pervasiveness offers a unique opportunity: the transformation of the communication infrastructure into a vast, distributed environmental sensing grid [2]. This paradigm shift envisions the optical network not

only as a data transport pipe, but as a multi-service, software-defined entity capable of monitoring both its own health and the surrounding environment. While recent studies have been focused on field trials in the undersea environment [3–6], there is huge interest in the investigation of sensing techniques in the terrestrial scenario [7–13]. In this case, typical meshed or ring topologies enable a smart-grid approach leveraging the large cross-correlation of data coming from diverse network sections. Moreover, the easier accessibility of the add-drop nodes to install additional sensors enables scalability to large geographical areas. As depicted in the architecture in Fig. 1, modern optical networks can exploit the streaming telemetry capabilities of deployed network elements (NEs) to retrieve

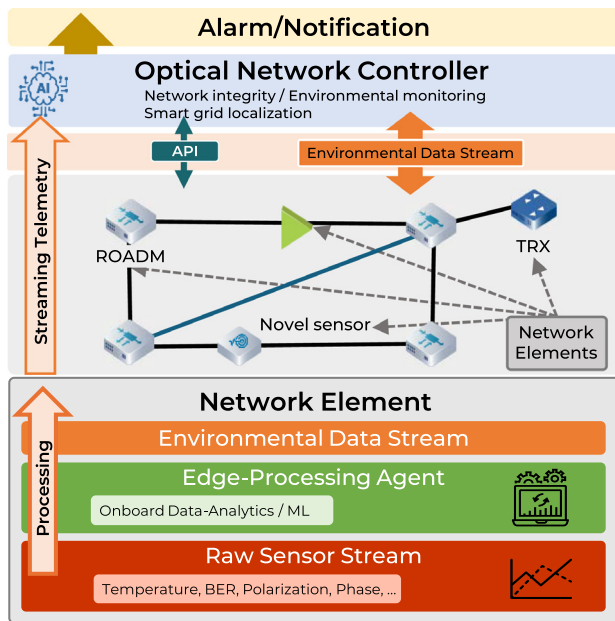


Fig. 1. Network sensing architecture: each network element produces telemetry data that can be processed in the edge and sent to a centralized controller for cross-correlation.

environmental information [14–16]. Unlike dedicated sensing solutions that often require dark fibers, this approach leverages the active components of the network—such as reconfigurable optical add-drop multiplexers (ROADMs), amplifiers, and transceivers, which are naturally equipped with embedded sensors [17]. These devices continuously monitor physical quantities like temperature, optical power, and the bit error rate (BER) for data network control and management purposes. Since these parameters are intrinsically sensitive to external stressors, they can be re-purposed to infer environmental conditions. Furthermore, to manage the vast amount of generated data, intelligent edge processing agents can be implemented directly at the NE level or within the node controller. Such an agent may send to the controller only a portion of the acquired signal when an event is detected or even just a timestamped notification to the centralized optical network controller (ONC). This allows for filtering significant data and transmitting only relevant features to the ONC, effectively enabling a scalable smart grid for wide-area monitoring. The ONC can take actions based on the sensing information received from network elements. For instance, if an earthquake is detected, the ONC can send an early warning alarm to the local seismic monitoring agency. Alternatively, when events that threaten the network infrastructure integrity are detected (such as fiber shaking or bending), the ONC can perform proactive network restoration actions such as establishing a backup lightpath to avoid service disruption. To enhance the sensitivity of this architectural framework beyond standard telemetry, specific sensing techniques based on the analysis of light propagation are required. While distributed acoustic sensing (DAS) offers high spatial resolution, its cost and need for dedicated fibers and spectral resources limit its deployment in active networks [18–20]. A more scalable alternative relies on monitoring the state of polarization (SOP) and the optical phase of the data

signals themselves. Optical fibers act as sensitive transducers; mechanical stresses, vibrations, and thermal variations induce birefringence changes and phase shifts that can be detected at the receiver [21]. Interferometric optical phase sensing loops back an optical carrier to detect the phase shift caused by the small path variations due to fiber deformation [12,22]. However, this typically requires expensive ultra-stable alien lasers [22] as an absolute phase reference. SOP monitoring instead does not require absolute phase references as it measures the differential phase between two orthogonal polarizations. Hence, this technique is particularly promising for mass deployment as it can be performed on standard intensity-modulated direct-detected (IMDD) signals, still widespread in the deployed networks, and using cost-effective detection devices like polarization beam splitters (PBSs) [23–26]. Such enhanced scalability comes with a cost. Unlike DAS, both interferometric phase and SOP monitoring techniques are not inherently spatially resolved as they provide the *integrated* effect over the fiber length. In this scenario, localization of an event along the fiber length is possible when the sensing technique is duplicated in the opposite propagation direction. One can then cross-correlate the two acquisitions to estimate the time delay between a perturbation caused by the same event and translate it to a position along the cable [23,27]. As dictated by the Cramer–Rao lower bound [28], the accuracy of this localization scheme scales down with the event’s signature signal-to-noise ratio (SNR), with its bandwidth, and as the time synchronization between the two opposite directions is less precise. While this solution may enable precise event localization concentrated at a specific point along the fiber, events such as earthquakes may trigger detection on multiple monitored fiber segments, thus enabling a coarse earthquake origin localization by triangulation using a smart grid approach. In this framework, smart grid localization does not rely on the intrinsic spatial resolution of a single sensing technique but emerges from the network-wide aggregation of measurements. By leveraging the meshed topology of terrestrial optical networks and the availability of synchronized telemetry streams, external perturbations can be localized through correlation of their signatures across multiple links and nodes. This enables a form of distributed inference, where the network itself acts as a sensing grid, and the localization accuracy depends on the spatial diversity and redundancy of the monitored paths. In this paper, which extends our work presented at ECOC 2025 [29], we take on the in-field implementation of this multi-technique sensing vision, with priority on the event detection. We shift the focus from single-parameter monitoring to the aggregated use of diverse physical quantities collected via a unified telemetry plane. The paper is organized into two main experimental sections. Section 2 describes a long-distance testbed connecting Ascoli Piceno and Teramo (Italy). Here, we analyze data from a live terrestrial network where interferometric phase sensing and PBS-based SOP monitoring coexist with data traffic. We propose an unsupervised anomaly detection framework capable of identifying signal anomalies automatically and that can be potentially integrated into the ONC or in the edge processing agent of relevant network nodes. Section 3 focuses on an urban scenario in the city of Turin. Utilizing a metropolitan fiber ring owned by GARR carrying live traffic,

we compare acquisitions using different sensing techniques, including coherent transceivers, polarimeters, and a simplified PBS-based SOP monitoring device. In that section, we explicitly showcase the correlation between sensing-specific metrics (SOP) and standard network telemetry data (BER, temperature), demonstrating the potential of the proposed sensing architecture. Finally, we report on controlled experiments using a robotic arm to simulate mechanical perturbations, validating the system's ability to detect and characterize complex urban anomalies [30].

2. ANOMALY DETECTION ON THE PHASE AND SOP SENSING TESTBED

In this section, we focus on the experimental activities carried out in a section of the regional network between the cities of Ascoli Piceno and Teramo owned by Open Fiber. The proposed anomaly detection framework operates on data acquired from a multi-technique fiber sensing infrastructure deployed on a live terrestrial optical link. Two complementary sensing modalities are simultaneously employed along the same fiber cable: interferometric phase sensing and SOP monitoring. While both techniques probe mechanical perturbations acting on the fiber, they rely on different physical observables and exhibit distinct sensitivity and scalability characteristics.

A. Interferometric Coherent Phase Sensing

Interferometric phase sensing is based on the detection of optical phase fluctuations accumulated by a coherent optical carrier propagating along the fiber. External perturbations, such as seismic waves or anthropogenic vibrations, induce local strain and refractive index changes, resulting in measurable variations of the optical phase. By comparing the phase of the received signal with a stable local reference, it is possible to retrieve a time-resolved measurement of the integrated deformation experienced by the fiber. In this work, the probe for interferometric sensing is an ultra-stable laser (shown in the right panel of Fig. 2), following the approach described in [12,22]. The system employs coherent detection with sub-radian phase resolution and sensitivity to low-amplitude seismic signals over long distances. As previously mentioned, unlike conventional DAS, this technique is not able to pinpoint deformations along the cable. However, it features lower system complexity, data throughput, and cost, while typically operating on alien wavelengths in coexistence with data traffic also on ultra-long-haul links and still providing good sensitivity and frequency response. Similar to polarization-based sensing, the phase observable represents the line integral of fiber strain along the optical path and is therefore intrinsically non-localized. Nonetheless, its high signal-to-noise ratio makes it a reliable reference for validating detections obtained through complementary sensing approaches. The ADC can sample the photodiode output up to a frequency of 10 KHz. In the following, however, we employ such signals downsampled at 100 Hz [22].

B. PBS-Based State of Polarization Sensing

State of polarization sensing exploits the sensitivity of light polarization to mechanical perturbations acting on the fiber. External stress and bending induce birefringence variations, leading to measurable SOP fluctuations even in the absence of coherent detection. In the proposed setup (illustrated in the left panel of Fig. 2), SOP monitoring is realized using standard IMDD optical channels, such as optical supervisory channels, detected with a PBS and direct photodetection-based devices developed by the Italian optical transport solutions vendor SM-Optics [23,31]. Each SOP sensing unit splits the received optical signal into two orthogonal polarization components using a PBS, which are independently detected and digitized using two photodetectors and DC-coupled ADCs with 12 bit resolution and 100 Hz sampling frequency to retain slow variations. The digitized orthogonal components are then normalized with respect to the total received instantaneous power detected using a third photodiode and ADC in order to compensate for possible small total power variations. The two normalized orthogonal components are then subtracted to cancel out the common mode noise and enhance the fluctuations caused by dynamic polarization changes induced by environmental and anthropogenic disturbances. To date, the SOP signal is acquired in 12 h long sessions interrupted by a gap of about 2 min that are transferred daily to a remote data storage server. At a 100 Hz sampling frequency, each session takes around 90 megabytes of storage. We envision the implementation of a real-time streaming service in the near future as a step toward the sensing network architecture described in Fig. 1. The resulting measurement thus provides partial polarization information with respect to full-Stokes vectors acquired using a polarimeter and can be interpreted as the evolution of S_1 in the receiver polarization frame. This approach may exhibit lower sensitivity compared to interferometric phase sensing as this depends on the average SOP at the receiver, which nonetheless slowly changes in time, for example, due to the thermal variations. In particular, the sensitivity worsens as the average receiver polarization state fades from linearly polarized toward circularly polarized states. However, it offers significant advantages in terms of scalability, cost, and ease of integration into existing network infrastructure [29], as it does not require signal loop-back in the backward direction. This is a clear advantage with respect to DAS, which observes the Rayleigh back-scattered signal, thus limiting the deployment in the presence of an optical amplifier's optical isolators. With respect to the interferometric approach, full forward sensing avoids wasting spectral slots in the return fiber. The SOP sensing device can operate continuously on live traffic fibers and can be deployed at multiple network points of presence. These characteristics make it particularly attractive for large-scale, long-term sensing applications and motivate its use as a complementary observable within the proposed multi-tech anomaly detection framework.

C. Open Fiber Regional Cable Testbed

Figure 3 illustrates the geographical layout of the monitored terrestrial optical link used in this study. The experimental setup is deployed on a production regional network operated

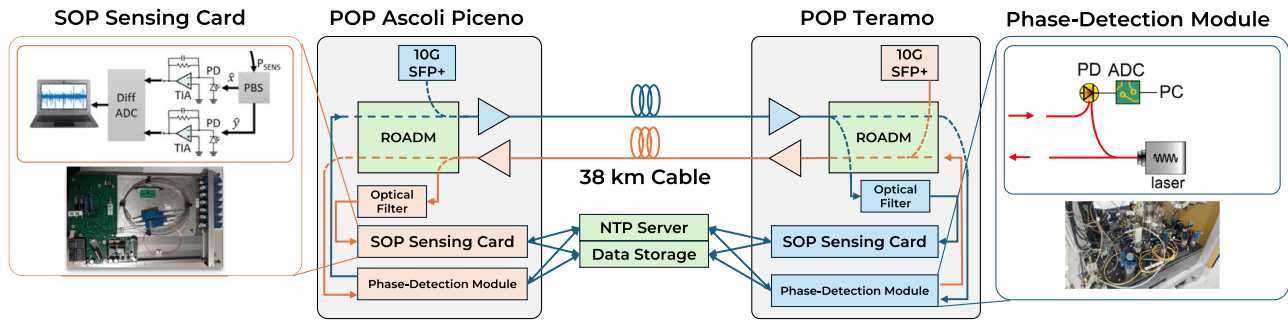


Fig. 2. Schematic overview of the experimental multi-technique sensing setup. The setup integrates the SOP sensing card (left) and the ultra-stable laser phase-detection module (right) on the same fiber cable (center).

by Open Fiber and consists of a bidirectional fiber cable connecting two network points of presence (POPs) located in central Italy. The two POPs are separated by approximately 39 km of optical fiber cable. Regarding the optical phase technique, the laser source is injected into one fiber within the cable at the Teramo POP and then looped back on a different fiber of the same cable at the Ascoli POP and received back at Teramo. The oppositely propagated phase signal was not available for this study. Regarding the SOP technique, a 10 Gbps commercial transceiver is used as a signal source launched into two different fibers of the same cable at each POP with -2 dBm power and received by the SM-Optics SOP sensing unit at the opposite POP. Both source signals are propagated within spectral slots made available by Open Fiber together with standard data signals partially loading the C-band. Unfortunately, we do not have access to the details of the overall spectral loading in each fiber. However, the infrastructure owner has not reported any significant degradation of the standard data signal transmission performance. A thorough study of the coexistence of such sensing signals and data channels is out of the scope of this paper. However, this scenario can be treated as the coexistence between coherent data channels and polarized continuous waves or IMDD data signals. Such a problem is commonly addressed by imposing a proper guard band between data and sensing signals [32]. The fiber route is predominantly buried inside underground conduits following road infrastructure, with the exception of a short aerial segment of approximately 100 m. This mixed deployment exposes the fiber to realistic environmental and anthropogenic perturbations, representative of typical terrestrial network conditions. As outlined in Fig. 2, both the interferometry and SOP detectors store their acquisitions on a remote server provided by Open Fiber, and their absolute time reference is obtained from the same Network Time Protocol (NTP) server.

D. Anomaly Detection

Fiber sensing systems deployed for long-term monitoring are continuously exposed to a wide range of perturbations, originating from both environmental forcing and human activities. Beyond seismic signals, the acquired data routinely include transient signatures associated with vehicle traffic, maintenance operations, or wind-induced oscillations of aerial cable spans or surrounding vegetation, among others. The automatic

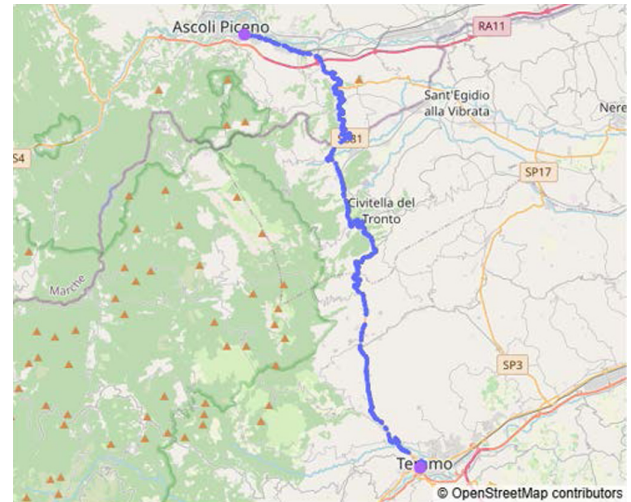


Fig. 3. Geographical layout of the Open Fiber terrestrial optical cable and location of the deployed sensing equipment.

detection of such events is a key requirement for infrastructural supervision and situational awareness, particularly in scenarios where continuous and quasi-real-time alerting is desired. Since the diversity and unpredictability of signal morphologies make supervised approaches impractical due to the need to collect large labeled training datasets, we investigate the use of unsupervised learning techniques that identify deviations from background behavior without relying on labeled datasets. Specifically, in this work, we adopt and extend an autoencoder-based anomaly detection framework to a multi-technique distributed sensing scenario, jointly addressing phase and SOP observables.

1. Signal Pre-Processing and Multi-Technique Alignment

Raw phase- and SOP-derived time series are first pre-processed to ensure consistency across sensing techniques. The two sensing systems are time-aligned using NTP, which delivers about 10 ms of accuracy. This level of accuracy is sufficient to compare the anomaly detection outcomes and assess that a perturbation detected using each method corresponds to the same event in time. Stricter synchronization may instead be required to localize the events across the fiber with a bidirectional, time delay estimation-based sensing setup [28], which is out of the

scope of this paper. Measurements are then interpolated onto a common temporal grid and downsampled to a sampling frequency of 100 Hz. This value represents a compromise between computational efficiency, data size, and the ability to resolve fast transients, such as impulsive anthropogenic events or short-lived environmental vibrations. This harmonization step enables the use of a unified machine learning architecture and detection logic for both sensing techniques, facilitating a direct comparison of their anomaly statistics and temporal response to the same physical perturbations. The simultaneous availability of interferometric phase and SOP measurements provides a redundant and synergistic view of fiber perturbations, increasing detection robustness and supporting cross-validation of automatically detected events.

2. Autoencoder-Based Anomaly Detection Pipeline

To detect anomalies within the continuous data streams without relying on manual labeling, we employ an unsupervised methodology centered on a dense autoencoder. A high-level schematic of the workflow is presented in Fig. 4. Following pre-processing, the time series are segmented via a sliding window with length w and unit step. A crucial aspect of our approach is the definition of the training set: to ensure the model exclusively learns the stationary background noise rather than transient disturbances, we implement a data-driven filtering strategy. All signal windows are sorted based on their root-mean-square (RMS) amplitude, and only the lowest 30%—representing the quietest periods—are utilized for the training phase. This enforces a robust definition of “normal” behavior. The neural network features a symmetric, fully connected architecture constrained by a low-dimensional bottleneck. Training is performed by minimizing the mean squared error (MSE) between the input window and its reconstruction. Once the model weights are frozen, the autoencoder is applied in inference mode across the entire dataset to identify deviations from the learned background.

3. Adaptive Thresholding and Event Post-Processing

During the inference stage, the reconstruction error is evaluated for every window. Because the sliding window approach results in overlaps where a single time sample is included in multiple windows, we derive a continuous, sample-wise anomaly score (AS). This is calculated by averaging the reconstruction errors across all k windows that cover a specific time

instant t :

$$AS(t) = \frac{1}{k} \sum_{i=1}^k (x_i(t) - \hat{x}_i(t))^2. \tag{1}$$

To distinguish genuine anomalies from the noise floor while accounting for slow environmental fluctuations, we apply a dynamic thresholding logic. We compute the moving average $\mu(t)$ and standard deviation $\sigma(t)$ of the AS over a 30 min horizon. A sample is flagged as anomalous if it exceeds the statistical bound defined by

$$AS(t) > \mu(t) + N\sigma(t). \tag{2}$$

For this field trial, we set $N = 5$ to balance sensitivity to small events against the rejection of false positives. Finally, a cleanup procedure transforms the raw per-sample triggers into a catalog of distinct physical events. This step involves filtering out negligible, extremely short-duration spikes and merging consecutive or closely spaced anomalous intervals into single logical entities.

E. Examples of Detected Events

Figures 5 and 6 show representative examples of anomalies detected by the proposed framework running on phase-based detection data. Both are recurring events that have been previously verified by on-site human inspection during the years of deployment of the sensing testbed. Figure 5 corresponds to the passage of two vehicles at around the 1 and 6 s marks. Each vehicle passage shows up as two sharp peaks caused by the front and rear wheel axles passing over a section of damaged asphalt, exposing the optical fiber cable. Peaks are clearly visible as distinct localized fast transients in both the raw signal and the derived anomaly score. The automatic detection accurately identifies the duration of both events without prior knowledge of their signatures. A second example, shown in Fig. 6, highlights wind-induced oscillations of an aerial fiber span interacting with nearby vegetation. The figure compares the SOP (top three panels) and interferometric phase (bottom three panels) across three domains: time series, time-frequency spectrograms, and the resulting anomaly scores. The perturbation, lasting approximately 120 s (from $t \approx 80$ s to $t \approx 200$ s), exhibits a quasi-periodic structure clearly visible in the spectrograms. While the interferometric phase spectrogram reveals sharp, well-defined harmonic lines extending up to 20 Hz, the SOP spectrogram displays a more diffuse

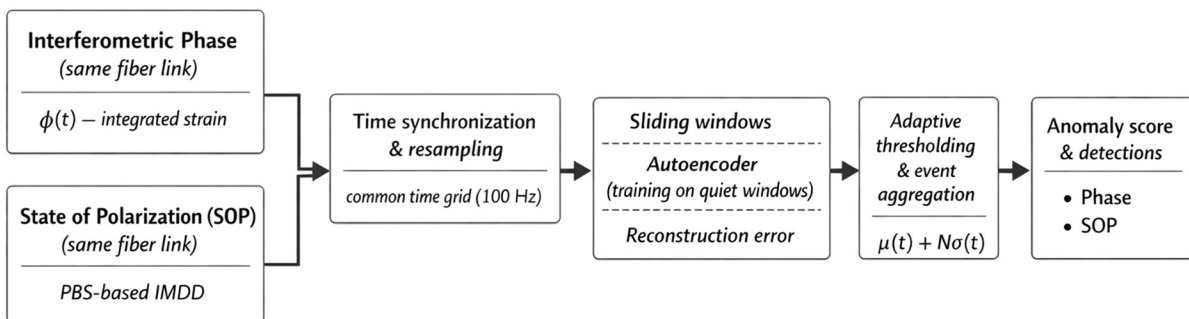


Fig. 4. Overview of the unsupervised multi-technique anomaly detection pipeline.

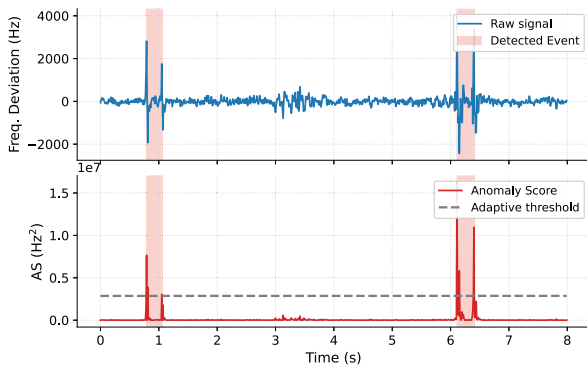


Fig. 5. Example of automatically detected passage of two vehicles in the phase trace.

spectral energy concentrated in the lower frequency range (<10 Hz). Identification of the source is based on these harmonic patterns, which correspond to the natural frequencies of a suspended cable. Such differences arise from the different nature of the compared sensing technologies. Interferometric phase is mostly sensitive to longitudinal fiber strain, while the SOP is also impacted by the cable transversal compression, which modulates the birefringence intensity. Moreover, even different fibers inside the same cable may exhibit different responses to the same event as that is strongly dependent on the cable coupling to the ground. Hence, a more detailed and quantitative investigation deserves dedicated observation that must be carried out in a controlled laboratory environment as the response is influenced by too many uncontrollable factors in a production testbed of several kilometers. Despite the different spectral signatures and SNRs, the derived anomaly scores (third and sixth panels) demonstrate that the unsupervised pipeline consistently detects the event, crossing the adaptive threshold synchronously in both modalities. These examples demonstrate the ability of the autoencoder-based detector to identify events of diverse physical origin without the need for manual labeling or explicit modeling assumptions.

1. Comparative Analysis between SOP and Interferometric Data

The availability of both SOP- and interferometry-based observables enables a direct comparison of their anomaly detection performance. Figure 7 shows a heatmap of anomaly counts per hour of the day of both techniques over the same observation period of two weeks, from 17 March 2025 to 30 March 2025. The two sensing modalities exhibit similar distributions of detected events, indicating that the proposed pipeline captures mostly genuine physical perturbations rather than technique-specific artifacts. At the same time, subtle differences in detection density suggest complementary sensitivities, which could be exploited for cross-validation or enhanced event characterization in future developments. For example, on Thursday the 27th at 21:00, the SOP exhibits 35 anomalies and no anomalies on the phase. Conversely, the phase counts 46 anomalies on Tuesday the 25th at 11:00 and 0 on the SOP. As previously mentioned, these differences may arise from the different underlying mechanisms of the

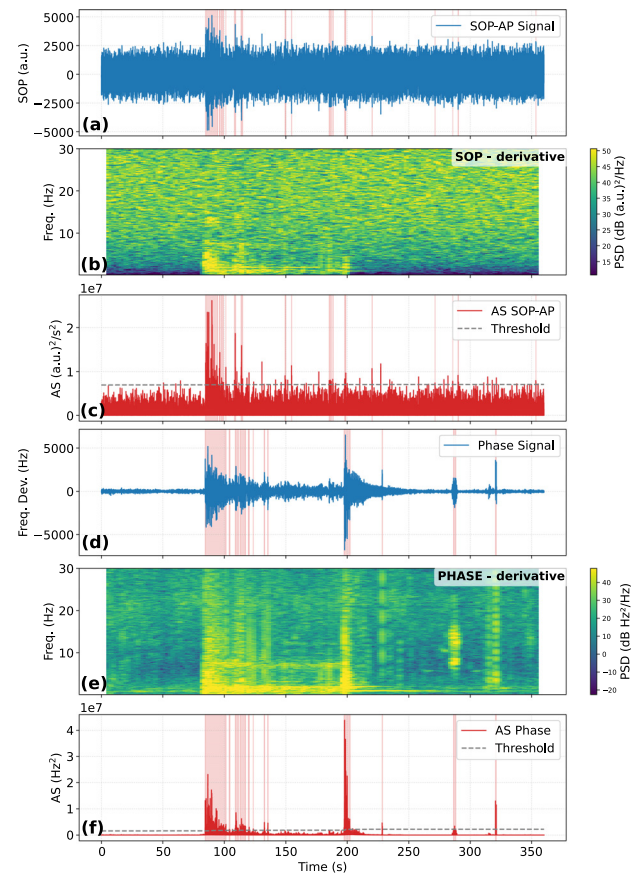


Fig. 6. Observation of the wind-induced oscillations of an aerial fiber span interacting with nearby vegetation. (a), (b), (c) The SOP time trace, spectrogram, and anomaly score, respectively, recorded at the Ascoli Piceno POP. (d), (e), (f) The interferometric phase frequency deviation time trace, spectrogram, and anomaly score, respectively.

two techniques and their sensitivity to the fiber to the ground coupling, showing how both can be used complementarily to enrich the set of detected anomalies.

3. MULTI-TECH SENSING ON THE TURIN URBAN TESTBED

In the previous section, we have shown a deployment of a multi-tech sensing testbed using coherent interferometry and the SM-Optics (SMO) PBS-based polarization sensing unit in an inter-urban scenario involving two cities. In this section, instead, we focus on the observation of the measurements obtained in different stages during the second half of 2025 on a second, urban-only, testbed deployed in the city of Turin. Here we use a metropolitan fiber ring owned by the GARR consortium [33] and involving transceiver Q-factor and full polarimeter-based sensing techniques to showcase their potential in an urban environment.

A. Metropolitan Ring Experimental Setup

The GARR metropolitan fiber cable is a 28.5 km long fiber ring deployed underground around the city center of Turin. Figure 8(c) shows the cable map, made up of three segments

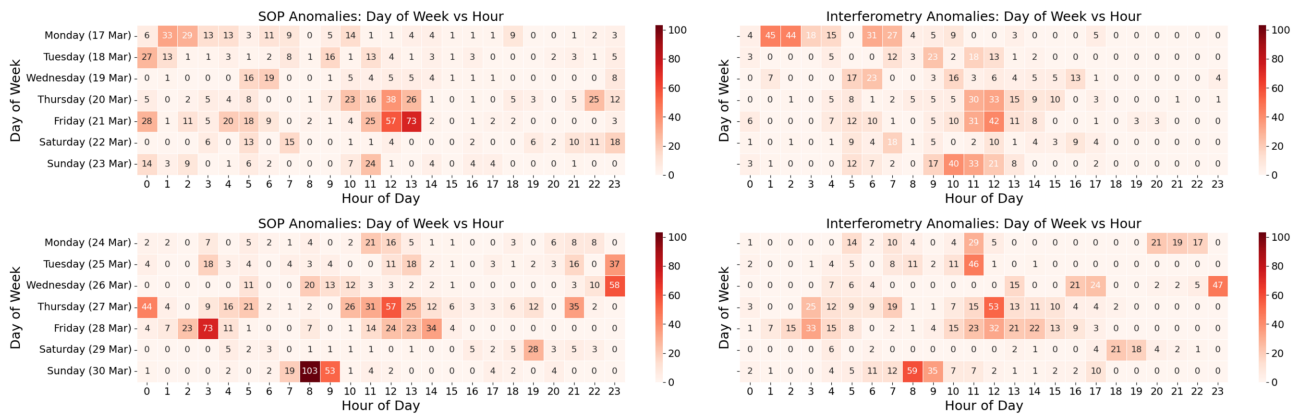
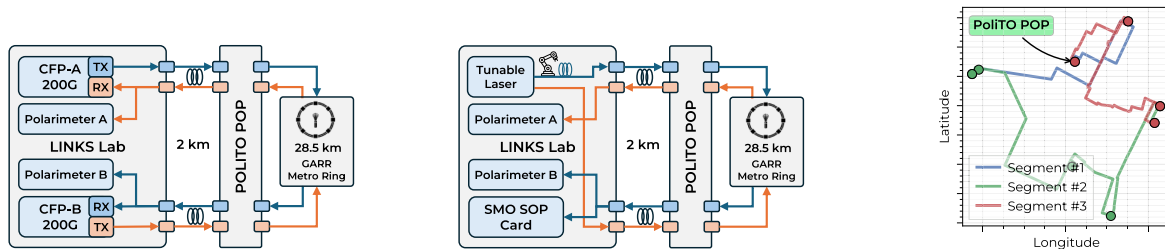


Fig. 7. Heatmaps of detected anomaly counts of SOP-based measurements (left column) and interferometric phase (right column) over the same observation period: the week of 17–23 March 2025 (top row), the week of 24–30 March 2025 (bottom row).



(a) Experimental setup 1 using coherent data signals source and 200G transceiver BER telemetry. **(b)** Experimental setup 2 using tunable laser source, SMO PBS-based SOP monitoring unit and robotic arm on the AB link. **(c)** Map of the GARR 28.5 km metropolitan ring.

Fig. 8. Block diagrams of experimental (a) setup 1 and (b) setup 2 at the LINKS laboratory. (c) Map of the GARR 28.5 km metropolitan ring.

(displayed with different colors) and the available POP. The actual geographical locations in the city are confidential. Cable access is possible from the POP located at Politecnico di Torino (PoliTO). The PoliTO POP is connected to the LINKS Foundation laboratory (Fig. 8) with a 2 km long fiber. Within the activities of several research projects, GARR made available a 100 GHz WDM slot in both propagation directions to carry out experimental activities. The rest of the spectrum is partially loaded with standard coherent data signals managed by GARR. Unfortunately, we do not have access to the detailed spectral load description. However, even in this scenario, GARR has not reported significant transmission penalties. Having access to the metro cable directly from the LINKS laboratories enabled much more flexibility and allowed us to perform acquisitions using different devices and techniques. In particular, here we consider the two setups reported in Fig. 8. In setup 1, we propagate two 200G signals in opposite directions through the fiber ring using the available 100 GHz slot. In the A-to-B (AB) direction, the signal travels in order through segments 1, 2, and 3 coming back to PoliTO POP; the opposite in the B-to-A (BA) direction. Data signals are generated by two commercial CFP-2 coherent transceivers hosted within a whitebox Galileo Phoenix transponder by NEC using DP-16QAM at 32 GBaud. After ring propagation, each signal is received back by the CFP-2 module at the LINKS laboratory, and the BER is stored and timestamped using NTP on our streaming telemetry platform with an average sampling frequency of 0.06 Hz (one BER sample every 16 s). Before

coherent detection, a portion of each received optical signal is tapped and fed to two Novoptel PM1000 polarimeters to retrieve and store the full Stokes vector time evolution. The polarimeters' sampling rate is set to 95 Hz, which is a good compromise between the capability to support long-time measurements and to detect anomalies generated by anthropic activity. We thus obtain two BER and Stokes vector streams measured from two coherent signals propagating in the same cable in opposite directions AB and BA. These measurements have been carried out during August 2025. Setup 2 instead has been employed during July and October 2025. In this case, the Stokes detection configuration remains the same as setup 1, while the source is changed. A tunable laser generates an unmodulated carrier at 1565.496 nm, which feeds both the propagation directions. After ring propagation, while the BA signal is fed to polarimeter A only, the AB signal is split and received by both polarimeter B and the SMO SOP device. We thus collect two polarimeter streams in opposite directions and one SMO SOP stream, both at 100 Hz. Due to the SMO device malfunctioning, however, we were able to collect only polarimeter traces during July acquisitions, while the SMO device was operative in October. We also employed a variation of setup 2 during the measurements of October 2025. In this scenario, at the tunable laser output in the AB direction only, we employed an Arduino-based robotic arm to simulate fiber shaking in a controlled environment. This variant was employed within another research activity focusing on the identification of mechanical disturbances, which

can impair telecom infrastructure integrity through SOP monitoring [30]. The robotic arm was configured to interact with the fiber through a vertical “shaking” motion, maintaining a 90° angle relative to the fiber’s longitudinal axis to maximize stress induction. We defined two specific mechanical regimes: “Slow Shaking” (1–5 Hz), mimicking manual cable handling and tapping, and “Fast Shaking” (5–10 Hz), which replicates the high-frequency transients associated with critical vibrations, which could possibly lead to fiber cut. Although both setups feature two oppositely propagated polarimeter acquisitions, it was not possible to exploit them to perform localization because the polarimeter timebase was not accurately synchronized, relying on only on a coarse NTP synchronization.

B. Experimental Data Analysis

We first focus on the observation of the experimental measurements using setup 1. Figure 9(a) shows the time series acquired from 1 August at 16:30 to 8 August at 4:30 (Europe/Rome timezone). Rather than showing the raw Stokes vector, we have preferred to rework the polarimeter acquisitions in the Jones domain. This allows us to observe the proper phase difference between orthogonal polarization components. The received electric field Jones vector \mathbf{J} can be expressed as

$$\begin{aligned}\mathbf{J} &= \begin{bmatrix} E_x \\ E_y e^{i\delta} \end{bmatrix}, \\ \delta &= \phi_y - \phi_x, \\ \alpha &= \frac{E_x}{E_y},\end{aligned}\quad (3)$$

where E_x and E_y are the orthogonal electric field components. ϕ_x and ϕ_y are their absolute phases. Thus δ is the phase difference between the orthogonal components, and α is the amplitudes’ ratio. These quantities are obtained from the Stokes vector using the following relations:

$$\begin{aligned}\alpha &= \arctan\left(\frac{1 - S_1}{1 + S_1}\right), \\ \delta &= \arctan\left(\frac{S_3}{S_2}\right).\end{aligned}\quad (4)$$

Together with the Jones parameters, Fig. 9(a) also shows the Q-factor in dB obtained from the simultaneously acquired transceivers’ BER:

$$Q = \sqrt{2} \operatorname{erfc}^{-1}(2 \cdot \text{BER}). \quad (5)$$

Coherent data signals are inherently depolarized, thus not having a fixed polarization state with equally distributed power between the orthogonal components and the degree of polarization (DOP) near zero. Hence, one may argue that observing their polarization state with a polarimeter should not deliver any meaningful information about external disturbances. However, the acquisitions show an oscillation on α with a one day period and several peaks that could be caused by human

or urban activities on the fiber cable. Upon further inspection on shorter timespans, here not reported for space constraints, the polarization measurements also show oscillations with a period ranging from 30 to 60 min and lasting for several hours. We may argue that variations with such periods are caused by cooling or some form of maintenance in the GARR PoPs. However, we cannot be sure of the validity of this hypothesis, as currently we do not have access to these locations or to the building’s internal temperature data. Moreover, Q-factor variations seem strongly correlated with the SOP, at least on longer periods. Hence, this suggests that observing a coherent channel SOP using a simple polarimeter, rather than accessing the transceiver estimated Jones matrix, can still provide precious data on environmental events. This is a significant advantage as the access to transceiver Jones matrices is not easy due to the closed nature of DSPs, and it enables SOP sensing, avoiding waste of spectral slots to transmit a dedicated laser source. This feature can be justified with the polarization-dependent loss (PDL) introduced by optical amplifiers and add-drop nodes along the lightpath increasing the residual DOP [34]. However, this mechanism may also cause sensitivity variation along the route that is difficult to isolate in a non-controlled environment such as a production cable. However, a back-to-back SOP measurement at the transponder output may help isolate this effect, as in the absence of PDL, one would expect minimal SOP variation. A deeper understanding of this effect thus deserves dedicated laboratory experiments, which will be targeted in future works. As an example, Fig. 10(a) reports a zoom of the largest event in Fig. 9(a) on 7 August, although more lower magnitude anomalies can be found upon zooming the time series. The temporal spectrogram plots show the sum ($S_{xx,1} + S_{xx,2} + S_{xx,3}$) of the three single Stokes vector components S_i spectrograms $S_{xx,i}$. In each spectrogram shown throughout this paper, lower energy components are clipped out to underline the significant spectral content. Upon inspection, the peak is actually a roughly 1 h long sequence of disturbances whose shape is similar to human-induced stressors in [7] and whose spectral content is mostly limited to about 10 Hz. We underline that this event should be likely to have happened somewhere along the cable since it is visible in both propagation directions and the LINKS laboratory was closed during the August measurements, while the university campus was mostly uncrowded due to the summer break. Moreover, the Q-factor shows performance changes synchronized to the SOP variations, thus confirming detectable correlations between SOP variations caused by external disturbances and typical telemetry metrics available from optical network elements. It is then interesting to compare the coherent channel-based acquisitions to those obtained using setup 2 employing a tunable laser as signal source to confirm the validity of the coherent-sourced SOP detection. In this session, only polarimeter acquisitions were available, and their time series are shown in Fig. 9(b), spanning from 2 July 2025 at 14:30 to 18 July at 14:30, thus providing more than two weeks of measurements. Data present three gaps that have been necessary to restart the acquisitions after polarimeter buffer saturation: from 14:20 to 18:10 on 4 July, from 8 July at 19:50 to 9 July at 14:30, and from 13 July at 16:15 to 14 July at 13:00. In δ calculation, the phase has been cumulatively

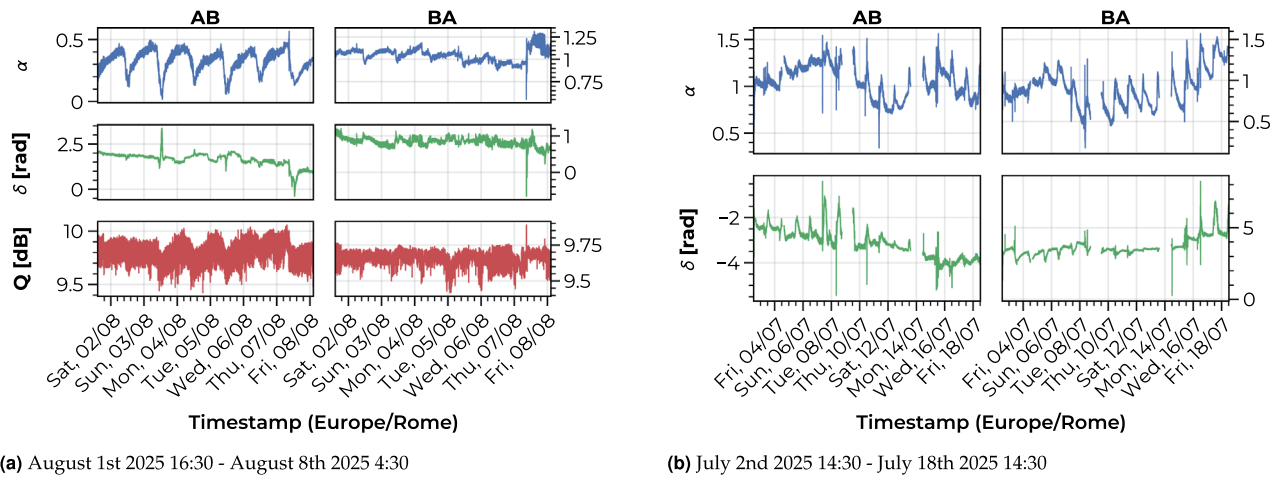


Fig. 9. Experimental measurements taken in (a) August 2025 using setup 1 and (b) July 2025 using setup 2 without an SMO card. Left columns: AB direction, right columns: BA direction. First/second rows: polarimeter Jones α and δ traces. Third (a) row: Q-factor (dB) from the transceiver BER. The time axis is shared, and each labeled tick corresponds to the day's midnight.

unwrapped assuming that no major phase variations happened during the gaps to preserve the visible trend in the long run. The overall July trend is comparable to the August acquisitions, thus validating the data acquired with a coherent source. The figures, however, show some different patterns between opposite propagation directions, which are more notable in the August polarimeter acquisitions, although the main trend and stronger peaks are in agreement. Inspection of the raw Stokes components, not shown here due to space constraints, shows that this major difference is caused by the average SOP being in different states between AB and BA in August, while the two directions in July remained steady around similar polarization states. With respect to the August acquisitions, however, the July set of measurements shows more anomalies as

the large peaks on 6, 7, and 10 July, while many more with different intensities can be observed upon further inspection. In Fig. 10(b), we report as an example the event of 10 July 2025 at 10:30. Even in this case, the peak is a sequence of perturbations of the parameters α and δ lasting around 5 min, which may suggest maintenance along the fiber path. The time evolution is compatible with the event of Fig. 10(a) with similar spectral content still limited to around 10 Hz. Regarding the slow variations with evident daily periodicity, we observe that while during July this trend also fades through the phase difference δ , in the August dataset it is strongly visible only through α because during this period the SOP varied along a circularly polarized state. In Fig. 11, we show that they are caused by the night and day temperature variations, reporting α and the

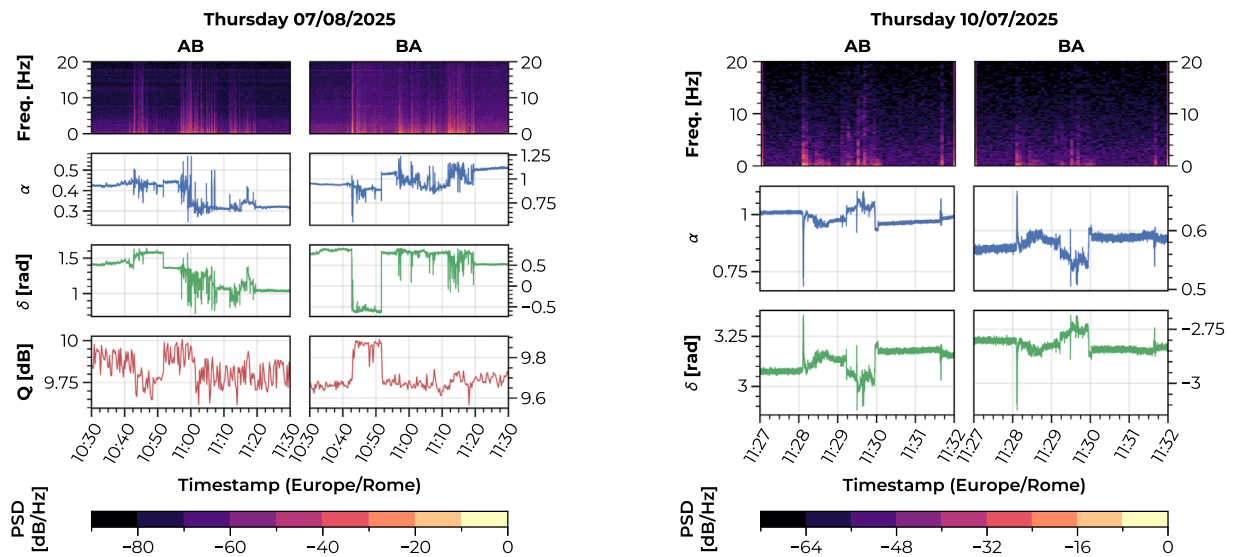


Fig. 10. Example of detected anomalies during the August and July 2025 acquisitions. (a) Event of Thursday 2025 August 7th, 10:30. Left column: AB direction, Right column: BA direction. 1st row: time spectrogram. 2nd/3rd rows: Polarimeter Jones α and δ traces. 4th row: Q-Factor (dB) from transceiver BER. (b) Event of Thursday 2025 July 10th, 11:27. Left column: AB direction, Right column: BA direction. 1st row: time spectrogram. 2nd/3rd rows: Polarimeter Jones α and δ traces.

Fig. 10. Example of detected anomalies during the August and July 2025 acquisitions.

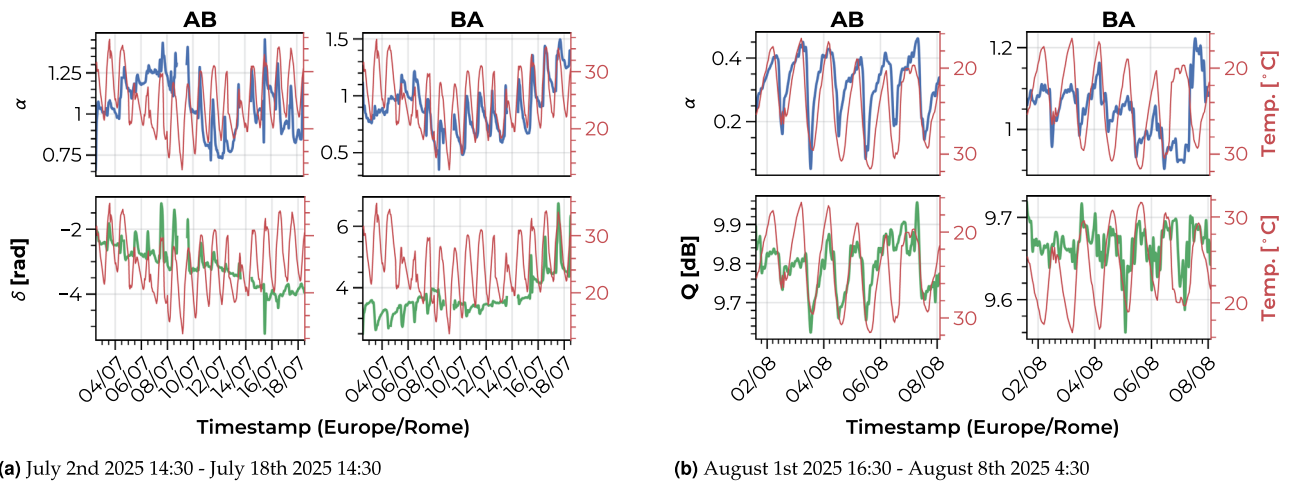


Fig. 11. SOP/Q-factor versus temperature taken in (a) July 2025 using setup 2 without an SMO card and (b) August 2025 using setup 1 filtered with a fourth-order Butterworth filter with 14 mHz bandwidth. Left columns: AB direction, right columns: BA direction. First rows: polarimeter Jones α trace, second (a) row: polarimeter Jones δ trace, second (b) row: Q-factor in dB from the transceiver BER. The left y axes show the recorded temperature (Celsius) of a nearby weather station. The time axis is shared, and each labeled tick corresponds to the day's midnight.

Q-factor for the August dataset and both α and δ for the July dataset. All the signals have been filtered using a fourth-order Butterworth low-pass filter with a cut frequency of 14 mHz in order to retain variations within a 2 h period. On top of them, we reported the temperature evolution obtained using the Open-Meteo API [35] from a weather station located in the city center of Turin and sampled every hour. The results show a very good match between the temperature curve and both the SOP and Q-factor features, thus also showing the dependence of transmission performance on daily temperature excursion. It is worth noting the opposite polarity of the August and July SOPs with respect to the temperature and of the AB Q-factor with respect to the BA Q-factor. This can be explained by the transition of the signal between opposite polarization states, from left circular to right circular polarization, for example.

We finally tackle the acquisitions carried out during October 2025 using setup 2. In this case, no long-term continuous measurements have been carried out. We thus show a subset of the observed events as the availability of the SMO PBS-based sensing unit enables testing of a multi-tech sensing scenario and the comparison to the reference polarimeter measurement. The SMO time traces show the difference between the two raw ADC counts as depicted in the PBS-based device block diagram in Fig. 2. Figure 12 shows a 20 s perturbation detected on 15 October 2025. The robotic arm was deactivated during this acquisition; thus, we are able to test the SMO device's capability to detect the event alone. Even in this case, the polarimeter trace is similar to the events previously seen in Fig. 10. The SMO device (receiving the AB signal) is able to detect the event and shows a time trace compatible with the polarimeter phase difference δ , although with opposite polarity. Both polarimeter and SMO spectrograms are compatible with the event spectral content below 40 Hz. In Fig. 13, we show instead two time windows where an anomalous external perturbation struck while the robotic arm was shaking the fiber to emulate perturbation caused by human activities in construction sites, which may be harmful to telecom infrastructure

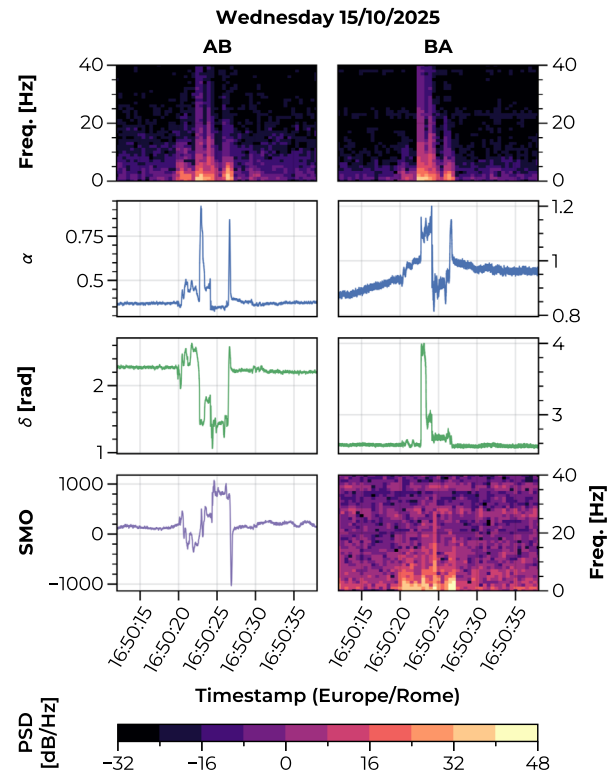
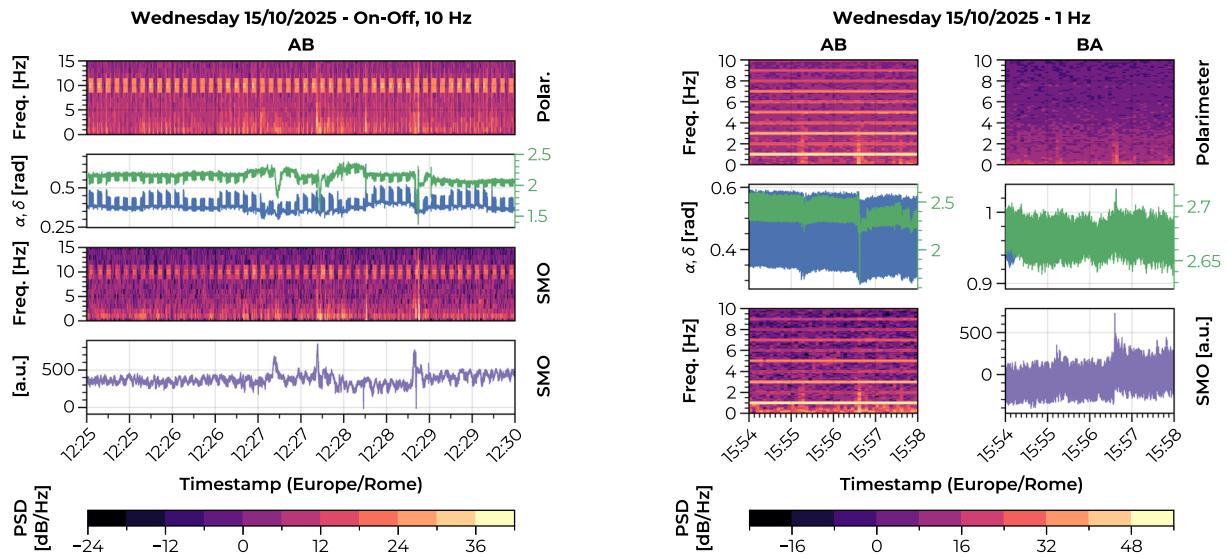


Fig. 12. Event on Wednesday, 15 October 2025 at 16:50. Left column: AB direction, right column: BA direction. First row, time spectrogram; second/third rows, polarimeter Jones α and δ traces; and fourth row, SMO device time trace (left) and time spectrogram (right).

integrity. Figure 13(a) shows the polarimeter and SMO device acquisitions between 12:25 and 12:30 on 15 October. In this case, the BA polarimeter acquisition was not available. The robotic arm shakes the fiber at 10 Hz intermittently every 3 s. While the SMO device time trace seems noisy, frequency analysis reveals the intermittent pattern of 10 Hz shaking,



(a) Event of Wednesday 2025 October 15th, 12:25 (AB direction only). 1st: Polarimeter time spectrogram. 2nd: Polarimeter Jones α (blue) and δ (green) traces. 3rd: SMO device time spectrogram. 4th: SMO device time trace.

(b) Event of October 15 2025, 15:54. Left column: AB direction, Right column: BA direction. 1st row: Polarimeter spectrograms. 2nd row: Polarimeter Jones α (blue) and δ (green) traces. 3rd row: SMO device time trace in the AB direction (right) and spectrograms (left).

Fig. 13. Events detected on 15 October 2025 using a polarimeter and an SMO PBS-based SOP monitoring device with the AB fiber shaken by a robotic arm. (a) Intermittent shaking every 3 s at 10 Hz, (b) continuous shaking at 1 Hz.

thus enabling detection upon proper filtering. Moreover, three anomalies happening from 12:27 to 12:29 are clearly detected by both sensing methods. Finally, Fig. 13(b) shows both directions of polarimeter acquisition together with the SMO device trace between 15:54 and 15:58 on 15 October 2025. As per Fig. 8(b), the arm excites only the AB fiber so that the BA polarimeter acquisition has not been impaired. Here the robotic arm continuously shakes the fiber with a frequency of 1 Hz. Both the polarimeter and SMO time spectrograms show the 1 Hz fundamental tone carrying most of the energy and several harmonics up to 10 Hz, and further, although we have limited the frequency axis to 10 Hz for cleaner visualization. However, also upon time traces inspection, two anomalies at around 15:55 and 15:57 struck while the robotic arm was shaking the fiber. These are still clearly visible in the spectrogram. Moreover, they appear on the BA polarimeter trace, which is not impaired by the robotic arm’s shaking. This enables the possibility to selectively detect, validate, and possibly localize anomalies by cross correlation of different signals measured at different points along the network and impaired by diverse phenomena.

4. CONCLUSION

In this work, we presented an in-field demonstration of a multi-technique sensing framework operating on live terrestrial optical networks. By exploiting the synergy between interferometric phase sensing and SOP monitoring, we shifted the focus from single-parameter observation to an aggregated sensing approach that leverages the pervasive nature of the optical infrastructure. We validated an unsupervised anomaly detection pipeline based on autoencoders using data from the long-distance Ascoli–Teramo testbed. This framework

proved capable of automatically identifying anomalies across different physical observables—phase and polarization—without relying on large, manually labeled datasets, ensuring robustness against environmental variability. Furthermore, the experimental activities conducted in the Turin metropolitan area highlighted the potential for correlation of specialized sensing metrics with standard network telemetry data, such as the transceiver Q-factor. Moreover, results showed that measuring the polarization evolution of a coherent data signal hooking up a polarimeter can provide an alternative and useful SOP data source, despite the depolarized nature of the coherent signals. The cross-validation performed using coherent transceivers, polarimeters, and cost-effective PBS-based devices confirmed the reliability of the proposed scalable solutions, while controlled experiments with a robotic arm demonstrated the capability to detect and characterize complex events. All demonstrated techniques operated in coexistence with data traffic, confirming the feasibility of transforming the optical transport infrastructure into a pervasive, distributed sensing grid. The move toward a unified telemetry plane that aggregates heterogeneous data sources—from high-precision phase sensors to standard network elements—paves the way for the implementation of cognitive, dual-purpose networks capable of simultaneous data transmission and environmental supervision.

Funding. EU Horizon project SENSEI (101189545); Open Fiber.

Acknowledgment. Portions of this work were presented at ECOC 2025 in Copenhagen, Th.02.05.2. We acknowledge GARR for the crucial support in making available the metro fiber ring.

Disclosures. The authors declare no conflicts of interest.

Data availability. Data underlying the results presented in this paper are not publicly available at this time but may be obtained from the authors upon reasonable request.

REFERENCES

1. D. Brake, "Submarine cables: critical infrastructure for global communications," Tech. Rep. (Information Technology and Innovation Foundation (ITIF), 2019).
2. J. S. Wey, "Distributed fiber optic sensing (DFOS) in telecom networks: industry trends and standards development," *J. Lightwave Technol.* **44**, 861–867 (2026).
3. A. Mecozzi, C. Antonelli, M. Mazur, *et al.*, "Use of optical coherent detection for environmental sensing," in *European Conference on Optical Communication (ECOC)* (Optica Publishing Group, 2022), paper Tu3D.1.
4. M. Mazur, J. C. Castellanos, R. Ryf, *et al.*, "Transoceanic phase and polarization fiber sensing using real-time coherent transceiver," in *Optical Fiber Communication Conference (OFC)* (Optica Publishing Group, 2022), paper M2F.2.
5. L. Costa, S. Varughese, P. Mertz, *et al.*, "Localization of seismic waves with submarine fiber optics using polarization-only measurements," *Commun. Eng.* **2**, 86 (2023).
6. A. Sladen, D. Rivet, J.-P. Ampuero, *et al.*, "Distributed sensing of earthquakes and ocean-solid Earth interactions on seafloor telecom cables," *Nat. Commun.* **10**, 5777 (2019).
7. C. J. Carver and X. Zhou, "Polarization sensing of network health and seismic activity over a live terrestrial fiber-optic cable," *Commun. Eng.* **3**, 91 (2024).
8. S. Pellegrini, L. Minelli, L. Andrenacci, *et al.*, "Overview on the state of polarization sensing: application scenarios and anomaly detection algorithms," *J. Opt. Commun. Netw.* **17**, A196–A209 (2025).
9. R. Bratovich, F. Martinez R., S. Straullu, *et al.*, "Surveillance of metropolitan anthropic activities by WDM 10G optical data channels," in *European Conference on Optical Communication (ECOC)* (Optica Publishing Group, 2022), paper Tu3B.6.
10. K. S. Y. Skarvang, S. Bjørnstad, E. Sæthre, *et al.*, "Local wind impact sensing using state of polarization measurement on a live short-haul aerial fibre cable," in *Optical Fiber Communication Conference (OFC)* (Optica Publishing Group, 2024), paper Tu2J.5.
11. P. Boffi, "Sensing applications in deployed telecommunication fiber infrastructures," in *European Conference on Optical Communication (ECOC)* (Optica Publishing Group, 2022), paper Mo4A.4.
12. G. Marra, C. Clivati, R. Luckett, *et al.*, "Ultrastable laser interferometry for earthquake detection with terrestrial and submarine cables," *Science* **361**, 486–490 (2018).
13. A. Bogris, T. Nikas, C. Simos, *et al.*, "Sensitive seismic sensors based on microwave frequency fiber interferometry in commercially deployed cables," *Sci. Rep.* **12**, 14000 (2022).
14. E. Virgillito, S. Straullu, F. Aquilino, *et al.*, "Detection, localization and emulation of environmental activities using SOP monitoring of IMDD optical data channels," in *23rd International Conference on Transparent Optical Networks (ICTON)* (2023).
15. F. Usmani, A. D'Amico, S. Straullu, *et al.*, "A smart sensing grid for road traffic detection using terrestrial optical networks and attention-enhanced bi-LSTM," *J. Lightwave Technol.* **43**, 4624–4634 (2025).
16. G. Malik, M. U. Masood, R. Ambrosone, *et al.*, "Demonstration of real-time AI-enabled smart fault detection using state-of-polarization monitoring," in *25th Anniversary International Conference on Transparent Optical Networks (ICTON)* (IEEE, 2025).
17. C. Jia, T. Pan, Z. Bian, *et al.*, "Rapid detection and localization of gray failures in data centers via in-band network telemetry," in *IEEE/IFIP Network Operations and Management Symposium (NOMS)* (2020).
18. B. G. Gorshkov, A. E. Alekseev, M. A. Taranov, *et al.*, "Low noise distributed acoustic sensor for seismology applications," *Appl. Opt.* **61**, 8308–8316 (2022).
19. P. J. Winzer, D. T. Neilson, and A. R. Chraplyvy, "Fiber-optic transmission and networking: the previous 20 and the next 20 years-invited," *Opt. Express* **26**, 24190–24239 (2018).
20. N. J. Lindsey, T. C. Dawe, and J. B. Ajo-Franklin, "Illuminating seafloor faults and ocean dynamics with dark fiber distributed acoustic sensing," *Science* **366**, 1103–1107 (2019).
21. Z. Zhan, "Distributed acoustic sensing turns fiber-optic cables into sensitive seismic antennas," *Seismol. Res. Lett.* **91**, 1–15 (2020).
22. S. Donadello, C. Clivati, A. Govoni, *et al.*, "Seismic monitoring using the telecom fiber network," *Commun. Earth Environ.* **5**, 178 (2024).
23. S. Straullu, F. Aquilino, R. Bratovich, *et al.*, "Real-time detection of anthropic events by 10G channels in metro network segments," in *IEEE Photonics Conference (IPC)* (2022).
24. P. Barcik and P. Munster, "Measurement of slow and fast polarization transients on a fiber-optic testbed," *Opt. Express* **28**, 15250–15257 (2020).
25. K. S. Y. Skarvang, S. Bjørnstad, and D. R. Hjelle, "A practical approach to vibration monitoring on a metro length fiber cable using low-cost state of polarization monitoring," in *IEEE Photonics Society Summer Topicals Meeting Series (SUM)* (2023).
26. B. Yang, H. Yu, Y. Yan, *et al.*, "Accurate vibration recognition enabled by synergistic sensing based on both phase and SOP for stable IM-DD optical interconnects," *J. Opt. Commun. Netw.* **18**, B85–B96 (2026).
27. C. Clivati, S. Donadello, F. Levi, *et al.*, "Proactive sensing of environmental events through optical data networks: a path to intelligent resilience," in *Proceedings of the European Conference on Optical Communications* (2025).
28. H. Cramér, *Mathematical Methods of Statistics*, Goldstine Printed Materials (Princeton University, 1946).
29. E. Virgillito, F. Notarstefano, R. Centonze, *et al.*, "In-field demonstration of multi-tech sensing on terrestrial optical data network using state of polarization and phase monitoring," in *Proceedings of the European Conference on Optical Communication (ECOC)*, Copenhagen, Denmark, 2025.
30. G. Malik, I. C. Dipto, M. U. Masood, *et al.*, "Resilient anomaly detection in fiber-optic networks: a machine learning framework for multi-threat identification using state-of-polarization monitoring," *AI* **6**, 131 (2025).
31. H. Awad, F. Usmani, S. Straullu, *et al.*, "Experimental validation for early earthquake detection using transfer learning," in *Optical Fiber Communication Conference (OFC)* (Optica Publishing Group, 2025), paper M1C.5.
32. E. Virgillito, A. Castoldi, S. Straullu, *et al.*, "QoT computation for 100G lightpaths routed on 10G-loaded dispersion-managed network segments," in *International Conference on Electrical, Communication, and Computer Engineering (ICECCE)* (2021).
33. Consorzio GARR, "La rete italiana dell'istruzione e della ricerca" (2026).
34. L. E. Nelson, C. Antonelli, A. Mecozzi, *et al.*, "Statistics of polarization dependent loss in an installed long-haul WDM system," *Opt. Express* **19**, 6790–6796 (2011).
35. Open-Meteo, "Free Weather API" (2026).